Inorganic Chemistry

Article

pubs.acs.org/IC

Structures of Delithiated and Degraded $LiFeBO_3$, and Their Distinct Changes upon Electrochemical Cycling

Shou-Hang Bo,[†] Kyung-Wan Nam,[‡,⊥] Olaf J. Borkiewicz,[§] Yan-Yan Hu,[∥] Xiao-Qing Yang,[‡] Peter J. Chupas,[§] Karena W. Chapman,[§] Lijun Wu,[#] Lihua Zhang,[▽] Feng Wang,[▼] Clare P. Grey,*[,†,∥] and Peter G. Khalifah*[,†,‡]

[†]Chemistry Department, Stony Brook University, Stony Brook, New York 11794, United States

[‡]Chemistry Department, [#]Condensed Matter Physics and Materials Science Department, [▽]Center for Functional Nanomaterials, [▼]Sustainable Energy Technologies Department, Brookhaven National Laboratory, Upton, New York 11973, United States

[§]X-ray Science Division, Advanced Photon Source, Argonne National Laboratory, Lemont, Illinois 60439, United States

[∥]Chemistry Department, Cambridge University, Cambridge CB2 1EW, United Kingdom

Supporting Information

ABSTRACT: Lithium iron borate ($LiFeBO_3$) has a high theoretical specific capacity (220 mAh/g), which is competitive with leading cathode candidates for next-generation lithium-ion batteries. However, a major factor making it difficult to fully access this capacity is a competing oxidative process that leads to degradation of the $LiFeBO_3$ structure. The pristine, delithiated, and degraded phases of $LiFeBO_3$ share a common framework with a cell volume that varies by less than 2%, making it difficult to resolve the nature of the delithiation and degradation mechanisms by conventional X-ray powder diffraction studies. A comprehensive study of the structural evolution of $LiFeBO_3$ during (de)lithiation and degradation was therefore carried out using a wide array of bulk and local structural characterization techniques, both in situ and ex situ, with complementary electrochemical studies. Delithiation of $LiFeBO_3$ starts with the production of Li_tFeBO_3 ($t \approx 0.5$) through a two-phase reaction, and the subsequent delithiation of this phase to form $Li_{t-x}FeBO_3$ ($x < 0.5$). However, the large overpotential needed to drive the initial two-phase delithiation reaction results in the simultaneous observation of further delithiated solid-solution products of $Li_{t-x}FeBO_3$ under normal conditions of electrochemical cycling. The degradation of $LiFeBO_3$ also results in oxidation to produce a Li-deficient phase D-Li_dFeBO_3 ($d \approx 0.5$, based on the observed Fe valence of ~2.5+). However, it is shown through synchrotron X-ray diffraction, neutron diffraction, and high-resolution transmission electron microscopy studies that the degradation process results in an irreversible disordering of Fe onto the Li site, resulting in the formation of a distinct degraded phase, which cannot be electrochemically converted back to $LiFeBO_3$ at room temperature. The Li-containing degraded phase cannot be fully delithiated, but it can reversibly cycle Li (D-$Li_{d+y}FeBO_3$) at a thermodynamic potential of ~1.8 V that is substantially reduced relative to the pristine phase (~2.8 V).

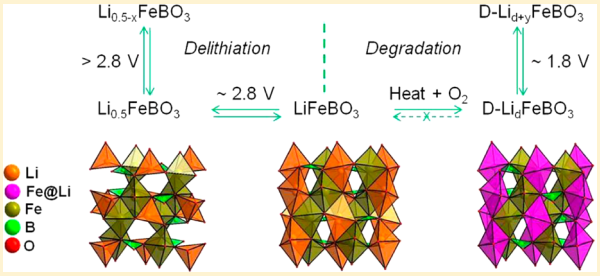

INTRODUCTION

Lithium-ion batteries are currently the major power sources for mobile electronic devices, and continue to hold promise for large-scale applications, such as electric vehicles, plug-in hybrid electric vehicles, and grid scale storage. These technological applications are driving a comprehensive search for new cathode materials that have high energy densities and safe operation voltages (below approximately 4.1 V vs Li^+/Li). $LiFeBO_3$ has emerged recently as a new cathode candidate for next-generation lithium-ion batteries.[1,2] In comparison to the commercialized compound $LiFePO_4$, $LiFeBO_3$ has a 30% larger theoretical capacity and an approximately 10% larger theoretical energy density. As is typical for oxoanion-based battery materials, the relatively low Fe^{3+}/Fe^{2+} redox potential is raised to commercially viable potentials due to the inductive effect produced by the oxoanion group (BO_3^{3-}) of $LiFeBO_3$. It also has the highest specific capacity of known oxoanion-based battery materials due to the low mass/charge (m/z) ratio of the BO_3^{3-} group. This promising material with an almost ideal element combination, however, suffers from poor rate capability and a relatively low operation voltage (~2.8 V; this and all subsequent voltages are relative to Li^+/Li). Detailed mechanistic knowledge about the redox processes in $LiFeBO_3$ is needed if the rate and voltage limitations of this compound[1,3] and its substituted variants[4,5] are to be understood and overcome.

Good room-temperature cycling behavior for $LiFeBO_3$ was only achieved after the existence of a degradation process was identified and steps were taken to minimize air exposure of

Received: January 22, 2014
Published: June 10, 2014

   dx.doi.org/10.1021/ic500169g | Inorg. Chem. 2014, 53, 6585−6595

$LiFeBO_3$,[1] leading to greatly improved electrochemical performance relative to prior studies.[6] It was later determined that degradation results in the formation of a distinct phase with an as-yet unknown crystal structure that is expected to be closely related to that of the pristine $LiFeBO_3$ phase,[7] and which still contains Li based on ^{7}Li solid-state NMR data. In both cases, it was found that degradation occurs very quickly when nano-$LiFeBO_3$ is exposed to air, and that this process occurs faster under modest heating (100−200 °C).

On delithiation, it has been clearly established that there is a ∼2% reduction in the unit cell volume of $LiFeBO_3$. Published diffraction data have thus far lacked the resolution and intensity needed to effectively distinguish between the delithiated and degraded phases, which are similar in cell dimensions and volume. Single-crystal diffraction experiments have recently demonstrated the existence of supercell in pristine $LiFeBO_3$ leading to a doubled *a*-axis and a four-dimensional space group of $C2/c(\alpha 0\gamma)00$ with $\alpha = 1/2$ and $\gamma = 0$[8] relative to the originally reported crystal structure.[6a] However, the subcell space group ($C2/c$) and lattice (a = 10.336 Å; b = 8.869 Å; c = 10.166 Å; β = 91.514°) are generally the most appropriate to use when modeling powder diffraction data because the strongest supercell reflection is about 3000 times weaker than the strongest subcell reflection, as judged from the X-ray diffraction structure factors. Unfortunately, this very small volume change makes it difficult to infer mechanistic insights (i.e., solid-solution vs two-phase) from the diffraction data published to date, which has been obtained on laboratory X-ray diffractometers.

The delithiation of the $LiFeBO_3$ was first reported to occur through a solid-solution mechanism with a continuum of phases $Li_{1-x}FeBO_3$.[1] The solid-solution mechanism was also suggested by density functional theory (DFT) calculations, based on the evaluation of the relative stabilities of $Li_{1-x}FeBO_3$ phases.[1] In a subsequent DFT study, the volume change between $LiFeBO_3$ and "$FeBO_3$" was predicted to be 1.4%, in reasonable agreement with experimental results.[9] It should be noted though that both DFT calculations were carried out using the originally published structure of $LiFeBO_3$ in the space group of $C2/c$ (No. 15) rather than the commensurately modulated structure. The modulation in $LiFeBO_3$ results in a long-range ordering of the one-dimensional (1D) LiO_4 tetrahedral chains that cannot be described in the originally proposed unmodulated $C2/c$ structure. This modulation modifies the configuration of the LiO_4 tetrahedra chains and thus alters the energy landscape of the $Li_{1-x}FeBO_3$ phases, although it is expected that the modulation will be absent in delithiated and degraded $LiFeBO_3$, both of which are formed through the loss of Li.

In contrast, later work suggested that the initial delithaition of $LiFeBO_3$ proceeds via a two-phase reaction based on galvanostatic intermittent titration technique (GITT) measurements with longer relaxation times.[7] It was not established whether this two-phase reaction persists across the full range of Li content with end members $LiFeBO_3$ and "$FeBO_3$", or whether intermediate compositions are formed. This remains an open question, due in part to the difficulty in fully relaxing the system to its equilibrium thermodynamic potentials at high states of charge.

A second unresolved question is the origin of the commonly observed low-voltage process (<2 V) during cycling of $LiFeBO_3$ that is manifested as a discrete plateau at ∼1.8 V in GITT data,[1,6b,7] but whose existence is also discernible in the curvature of other charge−discharge curves at low voltages. A typical $LiFeBO_3$ charge and discharge curve is shown in Figure 1. Starting with an open circuit potential of 2.8 V, charging the

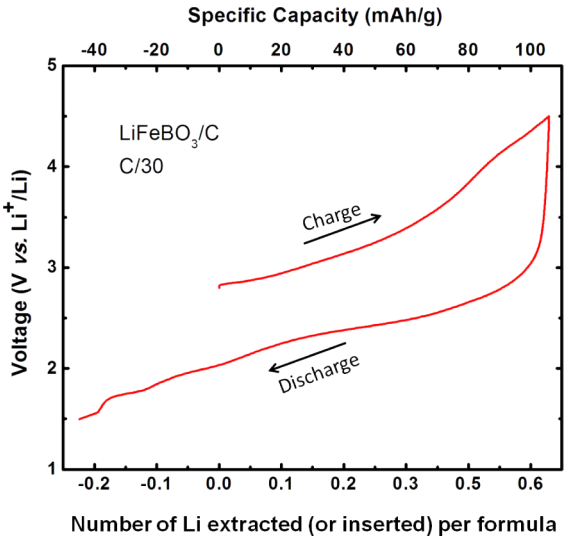

Figure 1. Electrochemistry of $LiFeBO_3$ at a rate of $C/30$ between 4.5 and 1.5 V. The number of Li extracted (or inserted) per formula was calculated on the basis of a full capacity of 176 mAh/g. The approximate valence of Fe was estimated on the basis of the assumption that iron was divalent after discharge, in accord with XANES results. See ref 7 for experimental details.

sample to 4.5 V results in a specific capacity of only 105 mAh/g, less than the expected full capacity of 176 mAh/g of this sample (80 wt % $LiFeBO_3$, 10 wt % Fe_3BO_5, and 10 wt % C). This charge capacity therefore corresponds to a removal of 0.6 Li per formula. The Li intercalation is clearly reversible, but surprisingly, an extra 0.2 Li can be accommodated in this system at voltages lower than 2 V. This process occurs at a potential of approximately 1 V lower than the Fe^{3+}/Fe^{2+} redox couple in $LiFeBO_3$ (∼2.8 V). It can in principle arise from either Fe conversion chemistry (the reduction of Fe^{2+} to Fe metal), a reaction with the degraded phase (designated D-Li_dFeBO_3), or a reaction with an amorphous phase that is formed at low voltage. It is important to identify the origin of this low-voltage process, which appears to be an integral part of the electrochemical activity of many $LiFeBO_3$ electrode preparations.

To resolve the complex evolution of structural and valence changes associated with $LiFeBO_3$ redox processes, we have used a wide range of complementary structural probes both in situ and ex situ that go beyond the normal repertoire of laboratory techniques. The in situ techniques included high-resolution synchrotron diffraction and synchrotron X-ray absorption fine structure measurements (XAFS). Also, solid-state nuclear magnetic resonance (NMR) was employed to probe the local environments of both Li and B ions during electrochemical cycling because structurally similar phases that are difficult to distinguish in diffraction can still give very different NMR signals if their electronic structures vary.[10] Neutron Bragg scattering and pair distribution function (PDF) analysis of total scattering data were used to probe differences in the structures of pristine and degraded $LiFeBO_3$ (D-Li_dFeBO_3). Finally, site occupancies of Fe and Li in the degraded phase were directly probed by high-resolution

dx.doi.org/10.1021/ic500169g | Inorg. Chem. 2014, 53, 6585−6595

transmission electron microscopy (HRTEM) imaging at single-particle level. On the basis of the analysis of results from these (and additional) complementary techniques, a model for the structural and valence changes in $LiFeBO_3$ during the distinct oxidative processes of delithiation and degradation is proposed. Furthermore, we demonstrate that degraded $LiFeBO_3$ is structurally distinct from the pristine $LiFeBO_3$ phase. The degraded phase is electrochemically active and is responsible for the reversible 1.8 V redox process, which first occurs during sample discharge (lithiation), because the as-formed degraded phase cannot be further delithiated.

EXPERIMENTAL SECTION

$LiFeBO_3$/C Composite. $LiFeBO_3$/C composite was prepared through the solid-state reaction of precursors under an actively reducing atmosphere of forming gas (5% H_2/95% N_2). In a typical synthesis, 3 g of powder precursors of Li_2CO_3 (Mallinckrodt, 99.0% min), $FeC_2O_4{\cdot}2H_2O$ (Alfa Aesar, 99%), and H_3BO_3 (Alfa Aesar, 99.5% min) were mixed in a stoichiometric ratio. Citric acid (Alfa Aesar, 99.5+%) was also added as the carbon source with a carbon content of no more than 20 wt %, where the 20 wt % assumption is based on carbon being produced from citric acid with 100% yield. The powder mixture was ball milled for 30 min in a SPEX SamplePrep8000 Mixer/Mill high energy ball mill by the use of a stainless steel jar. The resulting powder was then heated in a graphite crucible that was sealed in a tube furnace. After a dwell at 350 °C for 10 h, the temperature was ramped up to 650 °C under a heating rate of 100 °C h^{-1}, and kept at 650 °C for 20 h. Reaction products were removed from the furnace and immediately transferred to an argon glovebox. The $LiFeBO_3$/C nanocomposite typically contains ∼10 wt % Fe_3BO_5 as a major impurity based on X-ray diffraction (XRD) and ∼10 wt % C according to thermogravimetric analysis (TGA) results. A broad particle size distribution from a few nanometers to more than 100 nm was observed by scanning electron microscopy (SEM) and transmission electron microscopy (TEM). A thin surface layer of about 2−3 nm of amorphous carbon coating was seen in TEM images.[7]

Isotopic $^7LiFe^{11}BO_3$/C Composite and Degraded Isotopic $^7LiFe^{11}BO_3$. $^7Li^{11}BO_2$ was first synthesized by heating a ∼2 g powder mixture of $^7Li_2CO_3$ (Sigma-Aldrich, 99 atom % ^7Li) and $^{11}B_2O_3$ (ISOTEC, 99 atom % ^{11}B) at 750 °C in an alumina crucible for about 2 h with intermediate grinding. The isotopic $^7LiFe^{11}BO_3$/C composite was then synthesized in the same way as in the synthesis of nonisotopic $LiFeBO_3$/C composite. Degraded $^7LiFe^{11}BO_3$ was prepared by heating ∼1 g of powder of the as-prepared $^7LiFe^{11}BO_3$/C composite at 100 or 200 °C in air for 2−5 days.

Electrochemistry. Electrochemical testing was done in a 2032-type coin cell using an Arbin battery cycler. The electrolyte was 1 M $LiPF_6$ in a 1:1 volumetric mixture of anhydrous ethylene carbonate (EC) and anhydrous dimethyl carbonate (DMC). For the $LiFeBO_3$ cathode preparation, super P, polyvinylidene difluoride (PVDF), and 1-methyl-2-pyrrolidone (NMP, Sigma-Aldrich, 99.5%) were dried before use. First, 70 wt % active material, 20 wt % super P, and 10 wt % PVDF were mixed and ground thoroughly with NMP in an argon glovebox. This slurry was cast onto an Al foil and dried in a vacuum oven at 60 °C overnight. Circular disks with a diameter ∼14 mm were punched with a loading of ca. 5−10 mg of electrode materials. The current density was converted into a C rate on the basis of the $LiFeBO_3$ theoretical capacity of 220 mAh/g.

In Situ Fe K-Edge X-ray Absorption Spectroscopy (XAS). The Fe K-edge XAS was carried out in transmission mode at beamlines X18A and X18B at the Brookhaven National Laboratory's (BNL) National Synchrotron Light Source (NSLS) using a Si(111) double-crystal monochromator. The beam intensity was reduced by 30% to minimize high order harmonics. The XAS spectra were continuously collected while the in situ cell was charged and discharged in a voltage window of 1.5−4.5 V using a current density corresponding to $C/30$ rate. Reference spectra from a Fe metal foil were simultaneously collected for energy calibration. The X-ray absorption near edge spectra (XANES) data were processed using the Athena programs.[11] The extracted extended X-ray absorption fine structure (EXAFS) signal, $\chi(k)$, was weighted by k^2 to emphasize the high-energy oscillations and then Fourier-transformed in a k range from 3.0−13.0 Å using a Hanning window function to obtain magnitude plots in R-space (Å). The filtered Fourier transforms of EXAFS spectra in a R-range of 1.1−3.1 Å were fit using theoretical single scattering paths generated with the FEFF 6.0 ab initio simulation code, using the subcell structure of $LiFeBO_3$ ($C2/c$).[1]

In Situ High-Resolution X-ray Diffraction. Electrode pellets of the $LiFeBO_3$/C were prepared by mixing the active material with carbon black (Vulcan XC-72, Cabot Corporation), graphite SFG-6 (Alfa-Aesar), and PTFE binder (Sigma-Aldrich) in the mass ratio 6:1:1:2 and then pressing pellets (10 mm diameter, 120−150 μm thick) at an applied pressure of 1.6−1.8 ton. Pellets were assembled into the "AMPIX" electrochemical cell designed for in situ measurements.[12] Cells were cycled galvanostatically against lithium at a constant current of 7.3 mA/g ($C/30$), in the potential range of 4.5−1.5 V. High-resolution X-ray diffraction data were collected in transmission geometry at beamline 11-BM (λ = 0.4134 Å) of the Advanced Photon Source, at Argonne National Laboratory. Calibration of the instrument for wavelength, detector offsets, and instrument profile shapes was performed with a NIST SRM 660a (LaB_6). Data were collected using a multianalyzer detection assembly, consisting of 12 independent Si (111) crystal analyzers and $LaCl_3$ scintillation detectors, scanned between −2° and 12.0° at 0.12 s/step with 0.002° steps (14 min scan time). Data sets with $Q_{max} \approx 9$ $Å^{-1}$ were collected at 1 h intervals.

Neutron Bragg Diffraction and Pair Distribution Function. Time-of-flight (TOF) neutron Bragg diffraction data were collected at the POWGEN beamline of Spallation Neutron Source (SNS) at Oak Ridge National Laboratory (ORNL). Typically, ∼1.5 g of powder was packed into a 6 mm V can. Data were collected at a temperature of 300 K, with a proton pulse rate of 60 Hz. The data span a d spacing range of 0.41−3.61 Å, and were normalized against proton charge. A typical data collection time of 3−6 h was used. Neutron total scattering measurements were performed at the NOMAD beamline of the SNS at ORNL.[13] Typically, ∼100 mg of powder was packed into a 6 mm V can. One-hour scans were typically collected with a Q_{max} of ∼50 $Å^{-1}$. The pair distribution function (PDF) data were reduced and processed using scripts to normalize the data against a V spectrum from a 6 mm diameter V rod corrected for absorption, diffraction, and multiple scattering.

NMR. In the ^7Li magic angle spinning (MAS) NMR experiments, a 1.3 mm HX probe (Samoson) was employed on a Tecmag 200 MHz spectrometer with a 4.7 T magnetic field. A rotor-synchronized spin echo sequence ($\pi/2-\tau-\pi-\tau-$acquisition) was utilized, with a spinning speed of 50 kHz. The Larmor frequency of ^7Li is 77.71 MHz. A pulse width of 2 μs ($\pi/2$) was used. The recycle delay was 100 ms. 1 M LiCl was used as an external chemical shift reference (0 ppm).

The NMR spectra of paramagnetic materials are often broad, and analysis is made more complicated by overlapping spinning sidebands manifold even under fast magic angle spinning (MAS). A recently developed pulse sequence, projection-magic angle turning phase adjusted spinning sidebands (pj-MATPASS), was therefore employed to better resolve contributions from different phases.[14] For the pj-MATPASS experiments, the same probe was employed on a wide-bore Oxford 500 MHz (11.7 T) Varian Infinity Plus spectrometer, and a 50 kHz spinning speed was used. The pj-MATPASS pulse sequence was adopted from ref 14, and the starting t_1 was set to be 2/3 of a rotor period to minimize pulse ring-down effects before detection. The $\pi/2$ projection pulse was 1 μs, allowing a broad excitation of the spectra.

HRTEM. High-resolution TEM images were recorded from individual particles of the degraded phase, at 200 kV using a JEOL2100F microscope equipped with a Schottky field-emitter and a high-resolution pole-piece with a 0.23 nm point-to-point spatial resolution. To assist interpretation of the HRTEM images, image simulations were carried out using our own simulation codes based on the multislice method (E. J. Kirkland, Advanced Computing in Electron Microscopy, Plenum, New York, 1998).

dx.doi.org/10.1021/ic500169g | Inorg. Chem. 2014, 53, 6585−6595

RESULTS AND DISCUSSION

Phase Progression during $LiFeBO_3$ Cycling. A broad overview of the changes that occur in bulk $LiFeBO_3$ during cycling was obtained through in situ X-ray absorption fine structure measurements at the Fe K-edge. EXAFS measurements are most sensitive to local structure changes, while XANES measurements mostly probe Fe valence. As can be clearly seen in the data and fits to EXAFS spectra collected for the pristine, fully charged, and fully discharged samples, the local environment of Fe is minimally changed during electrochemical cycling of $LiFeBO_3$ (Figure 2).

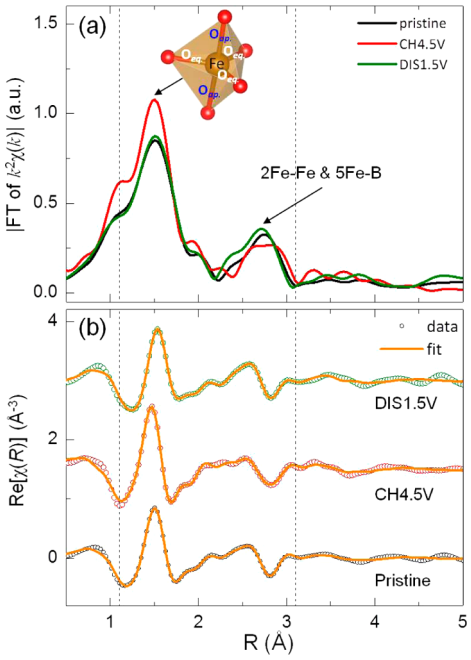

Figure 2. (a) Fourier-transformed EXAFS $\chi(k)$ magnitude spectra with k^2 weighting for pristine and cycled $LiFeBO_3$, fully charged to 4.5V ("CH4.5V"), and fully charged and then fully discharged to 1.5V ("DIS1.5V"). (b) Real part of the Fourier-transformed data for the same three scans along with the best fit (orange line). Broken lines indicate the range of the fit in real space (1.1–3.1 Å).

The magnitude of the Fourier-transformed (FT) EXAFS spectra for all three samples exhibits a strong peak at ~1.5 Å, which corresponds to the five Fe–O bonds in the FeO_5 trigonal bipyramids and another weaker and broader peak at ~2.7 Å that includes both Fe–Fe and Fe–B contributions (Figure 2a). Because the FT was not phase-corrected, the actual bond lengths are expected to be substantially longer (0.3–0.5 Å) than these values. Beyond these two FT peaks, no constructive contribution is observed above the noise level. There is no evidence for the formation of metallic Fe because the characteristic Fe–Fe correlations at 2.2 Å (not phase corrected) are not observed in the FT EXAFS spectrum of the fully discharged sample, thus refuting one hypothesis that Fe conversion chemistry (i.e., reduction of Fe^{2+} to Fe metal) may be responsible for the low voltage process observed during the electrochemical cycling of $LiFeBO_3$ (1.5–4.5 V).

Insights into the changes in the Fe–O coordination environment that occur during electrochemical cycling were obtained through least-squares fitting of the real-part of the EXAFS spectra (Figure 2b). The fitting procedure and best fit structural parameters are given in the Supporting Information (Table S1). The average Fe–O bond length for the pristine electrode is 2.04 Å. On charging to 4.5 V, this is reduced to 2.01 Å. The subsequent discharge increases the average Fe–O bond length to 2.06 Å. The average Fe–O distance in the fully discharged state appears to be even larger than that in the as-prepared electrode (2.06 vs 2.04 Å), indicating that the Fe valence has been reduced below its starting value after the discharge to 1.5 V.

The reduction in Fe valence after lithiation (discharge) can be directly resolved by following the shifts in the absorption edge in the XANES portion of the same in situ Fe K-edge X-ray absorption data. The progression of phases during the discharge process is presented in Figure 3. Three distinct

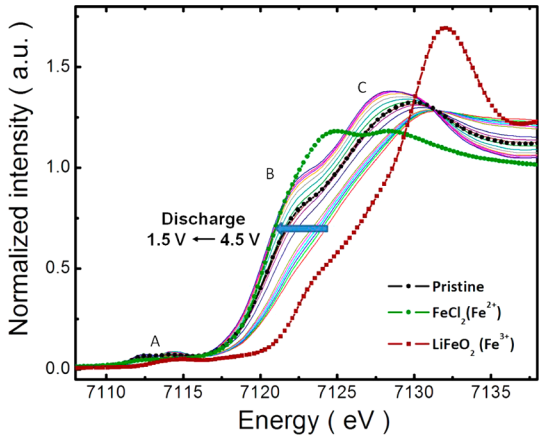

Figure 3. In situ XANES spectra of $LiFeBO_3$ during the discharge. The spectra of pristine $LiFeBO_3$ and the reference compounds ($Fe^{II}Cl_2$ and $LiFe^{III}O_2$) are shown for comparison.

edge features, marked as "A", "B", and "C", are observed in the XANES spectra (see the Supporting Information and Figure S1 for details). At the end of charge (4.5 V), the edge position (B) shifts to higher energy, in comparison to the pristine spectrum, indicating an increase in average Fe oxidation state approaching 3+ after the charge process. However, on the basis of comparisons with the edge position of reference spectra for $Fe^{II}Cl_2$ and $LiFe^{III}O_2$, Fe is not fully oxidized to Fe^{3+} after charging to 4.5 V, consistent with the incomplete Li extraction shown by the specific capacity (Supporting Information Figure S1). During discharge, the edge position (B) shifts back to lower energy, indicating a decrease of the average Fe oxidation state of $LiFeBO_3$. Interestingly, when discharged below 2.5 V (the XANES spectrum of discharged to 2.5 V overlaps with that of the pristine sample), the edge position shifts to energies that are even lower than the position of pristine $LiFeBO_3$. At the end of discharge, the edge position is almost identical to that of the reference $Fe^{II}Cl_2$ compound, suggesting that the electrode contains essentially just Fe^{2+}. This shows that the extra capacity obtained below 2.5 V during the first discharge is due to the reduction of higher valence iron species that existed in the original as-prepared electrode.

At first glance, there appeared to be several crossing points (circled in Figure S1 of the Supporting Information) in the XANES spectra during the first cycle, although a closer look reveals that these crossing points between successive scans shift in spectra that were collected near the end of charge and discharge, as highlighted in Supporting Information Figure S2. This suggests that two primary types of Fe local environments

dx.doi.org/10.1021/ic500169g | Inorg. Chem. 2014, 53, 6585–6595

are present during the cycling process, one associated with Fe^{2+} and the other associated with Fe^{3+}. The presence of crossing points at the early stages of charge might be taken to indicate that lithium extraction proceeds only via a two-phase reaction between $LiFeBO_3$ and $FeBO_3$, but our prior GITT data and current ^7Li NMR experiments (discussed below) strongly suggest that this is not the case. Difficulties in distinguishing between intermediate phases with very similar local environments have been seen in previous XAS studies,[15] a situation that is very applicable to the delithiated phases of $LiFeBO_3$ given the observed similarities in both the local Fe environment seen in the EXAFS spectra discussed previously and the very small changes in the unit cell lattice parameters determined from in situ XRD measurements (discussed later).

The local environment of Li can be directly probed by the complementary technique of ^7Li NMR because the ^7Li signal is influenced by both the coordination geometry and the valence of nearby Fe ions, and as such is able to very sensitively resolve the succession of phases that occur when $LiFeBO_3$ is cycled. The NMR responses from multiple phases ($LiFeBO_3$, $Li_{1-x}FeBO_3$, and D-Li_dFeBO_3) involved in the electrochemical processes are distinct, and their resonances and stoichiometry assignments will be discussed in the following two paragraphs.

^7Li MAS NMR spectra of $LiFeBO_3$ samples prepared by cycling equivalent batteries to different states of charge and discharge are shown in Figure 4. At the initial open circuit

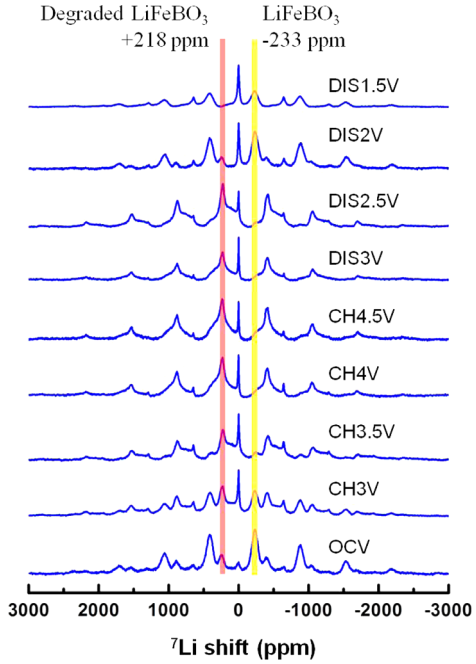

Figure 4. ^7Li MAS NMR spectra of $LiFeBO_3$ samples at different stages of cycling.

voltage (OCV), the sample is characterized by three ^7Li resonances, a $LiFeBO_3$ resonance at −233 ppm (yellow line) and two other resonances for secondary phases resulting from the degradation of $LiFeBO_3$, at +218 ppm (red line), the oxidized and degraded phase D-Li_dFeBO_3, and at 0 ppm, a Li-containing diamagnetic phase that contains the Li lost from the $LiFeBO_3$ lattice during degradation. These assignments were made in our previous study by studying samples with different overall contents of the degraded phase.[7] All of the other observed peaks are spinning sidebands, which are caused by partially averaging the anisotropic dipolar interaction between Li nuclei and unpaired electrons associated with Fe^{2+} and/or Fe^{3+} via the magic angle spinning. Note that any signals from residual electrolyte ($LiPF_6$) and the surface electrolyte interphase (SEI) found in the cycled samples are also diamagnetic and thus have resonances around 0 ppm. These contributions cannot be ignored in interpreting the intensity variation of 0 ppm signal.

During the cycling process, another broad feature assigned to the partially delithiated phase $Li_{1-x}FeBO_3$ appears (during charge) and disappears (during discharge) in the frequency regime around +218 ppm. This broad feature has a more positive hyperfine shift in comparison to the original $LiFeBO_3$ resonance (−233 ppm), suggesting that it is associated with Fe-containing phase with a higher oxidation state (i.e., >2).

During the first charge process to 4.5 V, the $LiFeBO_3$ resonance at −233 ppm rapidly decreases in intensity and has almost disappeared at 4.5 V when only 0.6 Li have been removed. There is no resolvable shift of the $LiFeBO_3$ resonance between the OCV and 4.5 V, in contrast to the shift or distribution of resonances that might be expected if a continuum of phases, that is, a solid-solution $Li_{1-x}FeBO_3$, existed. Also of note is that the broad feature assigned to Li in a partially delithiated ($Li_{1-x}FeBO_3$) lattice appears and grows as a shoulder to the right of the +218 ppm peak (∼100 ppm) at early stages of charge (CH3V with a removal of 0.15 Li and CH3.5V with a removal of 0.4 Li). This $Li_{1-x}FeBO_3$ resonance grows to its maximum intensity at around 3.5−4 V (∼0.5 Li removal), where the $LiFeBO_3$ resonance nearly disappears. It suggests that delithiation of $LiFeBO_3$ starts with a two-phase reaction whose other end member is suggested to be Li_tFeBO_3 with $t \approx 0.5$ based on capacity estimates and crystal chemistry arguments (represents the simplest periodicity that can be stabilized by charge order). The assignment of a $LiFeBO_3$−$Li_{0.5}FeBO_3$ two-phase region is also consistent with our prior GITT measurements, which indicate a clear 2.8 V plateau at both the beginning of charge and the latter stages of discharge.[7]

When the $LiFeBO_3$ battery is charged above 4 V, the broad feature shifts to more positive frequency (approximately +250 ppm) as signified by the appearance of a shoulder to the left of the +218 ppm peak. This further shifted resonance is therefore assigned to a further delithiated phase with a general solid-solution formula of $Li_{t-x}FeBO_3$ ($0 < x < t$). A closer look at the spectrum of CH4.5V reveals that a small portion of $LiFeBO_3$ still remains at the end of charge, indicating that the solid-solution reaction between $Li_{0.5}FeBO_3$ and $Li_{0.5-x}FeBO_3$ starts before $LiFeBO_3$ is fully converted to $Li_{0.5}FeBO_3$. This is consistent with the high overpotential (>0.5 V, Figure 1) needed to drive the delithiation of $LiFeBO_3$, and the relatively small potential difference between the electrochemical features associated with the $LiFeBO_3$−$Li_{0.5}FeBO_3$ two-phase reaction and the $Li_{0.5}FeBO_3$−$Li_{0.5-x}FeBO_3$ solid-solution reaction (∼0.25 V based on prior GITT data from first discharge).[7] The large overpotential is likely caused by either the broad size distribution of the pristine $LiFeBO_3$ particles where the core of bigger particles is difficult to delithiate due to transport limitations, or the appearance of secondary phases at the particle surface resulting from degradation or SEI formations that can impede Li^+ and/or e^- transport. All of the NMR hyperfine shift and intensity changes associated with the structural conversions between the pristine phase and the delithiated phases are reversed during the discharge (above 2 V), suggesting that phase progression is the same during charge

dx.doi.org/10.1021/ic500169g | Inorg. Chem. 2014, 53, 6585−6595

and discharge, a conclusion consistent with the observed electrochemical behavior of $LiFeBO_3$.

A separate experiment was carried out to determine if $LiFeBO_3$ can be fully delithiated to form "$FeBO_3$". Using a cutoff voltage of 4.5 V, a $LiFeBO_3$ battery was first galvanostatically charged to 4.5 V under a rate of $C/30$ and then held at 4.5 V until the current decayed to $C/3000$ about 2 days later (Figure 5). When the resulting product was studied

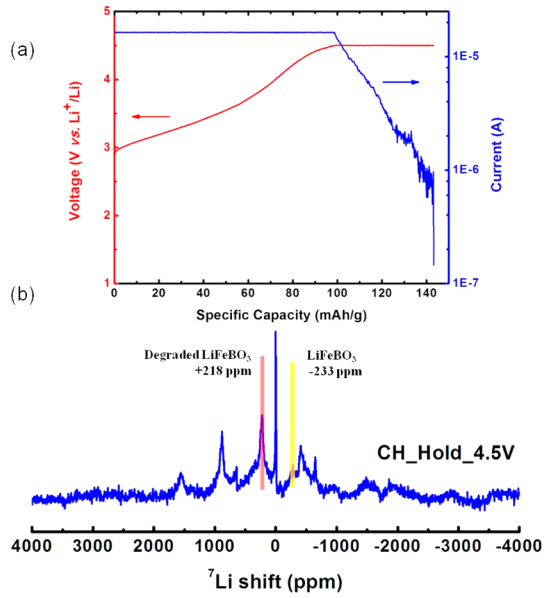

Figure 5. (a) Electrochemistry of a $LiFeBO_3$ sample charged to 4.5 V at a rate of $C/30$ and held at 4.5 V until the current decayed to $C/3000$ (axis of current is on a logarithmic scale). (b) ^7Li MAS NMR of the product after charging.

using ^7Li NMR to test if Li was still present in an iron borate lattice, the $Li_{0.5-x}FeBO_3$ resonance at ~250 ppm (left shoulder to the +218 ppm peak of the degraded phase) could still be seen, confirming that not all Li has left the lattice. This highlights the difficulty of fully delithiating $LiFeBO_3$ to form "$FeBO_3$" (up to 4.5 V). On the basis of the specific capacity, the final composition after the extended 4.5 V hold is estimated to be $Li_{0.2}FeBO_3$. Even after this extended high voltage hold, the degraded phase ^7Li resonance appears unchanged (same chemical shift, peak remains relatively sharp), suggesting that although Li is present in the degraded phase, this Li cannot be electrochemically extracted even under very harsh conditions (i.e., prolonged voltage hold at 4.5 V). However, it appears that lithium can be inserted into the degraded phase by discharging to low voltages (<2 V) because the intensity of the ^7Li NMR resonance at +218 ppm was reduced at 2 V and essentially disappeared at 1.5 V during the ex situ cycling experiments (Figure 4).

Synchrotron in situ XRD was used to follow the bulk structural changes of $LiFeBO_3$ during cycling (charge to 4.5 V, discharge to 1.5 V, and second charge to 3.5 V) under actual operating conditions without any of the relaxation phenomena associated with ex situ experiments. As seen in Figure S3 (Supporting Information), only very small changes in peak positions and intensities occur, suggesting that the structural framework of $LiFeBO_3$ is retained throughout the cycling. The diffraction data were analyzed through Rietveld refinements to extract two pieces of information: (1) the phase fractions of pristine and delithiated $LiFeBO_3$, and (2) the Li-content-dependent lattice parameter variations of delithiated $LiFeBO_3$. The structure of pristine $LiFeBO_3$ is very well-known from single-crystal X-ray diffraction experiments and was used without further refinement of atomic parameters or cell parameters, although the $C2/c$ approximant was used rather than the full $C2/c(1/200)00$ superspace group. Given the minimal changes in X-ray peak intensities during cycling and the very small scattering power of Li, B, and O, the same $LiFeBO_3$ structural model was also utilized to describe the partially delithiated phase (i.e., $Li_{1-x}FeBO_3$), and the lattice parameters of this phase were refined at each step during electrochemical cycling. As described in more detail in the Supporting Information, the fitting was further aided by (1) very effectively modeling the cell background in a parametric manner, and (2) utilizing a robust refinement algorithm[16,17] to minimize the adverse impact of components not formally included in the refinement (in particular, the variable composition degraded phase).

The phase fractions of three phases present in electrodes ($LiFeBO_3$, $Li_{1-x}FeBO_3$, and Fe_3BO_5) are shown in Figure 6,

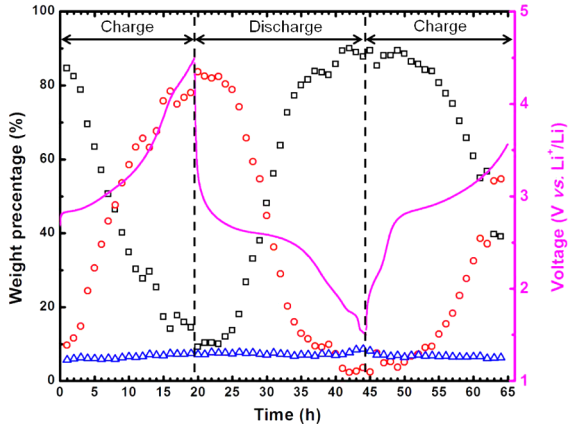

Figure 6. Weight percentages of $LiFeBO_3$ (black), $Li_{1-x}FeBO_3$ (red), and Fe_3BO_5 (blue) during cycling in the in situ run. The electrochemistry profile is shown in magenta with the voltage axis on the right.

while the graphical fits of some selected scans are presented in Figure S5 (Supporting Information). As expected, the fraction of the pristine phase decreases during the charge process (to a minimum value of ~10%) and increases during discharge, while the trend of the delithiated phase is inverted. Although freely refined, it can be seen that the mass fraction of the Fe_3BO_5 impurity remains constant (within 2%), indicating that the refinement is well behaved and that amorphization of the electrochemically active phases is not occurring. At voltages below 2 V, there is no change in the phase fractions of $LiFeBO_3$ and $Li_{1-x}FeBO_3$, indicating that the low voltage electrochemical processes (<2 V) do not involve $LiFeBO_3$, and instead result from electrochemically induced changes in the degraded phase D-Li_dFeBO_3, a conclusion confirmed by the ^7Li NMR data that are described in the Supporting Information (Figure S7).

The lattice parameters and unit cell volume of delithiated $Li_{1-x}FeBO_3$ at voltages above 2 V (where the weight percentage of the $Li_{1-x}FeBO_3$ phase is 10% or more) are plotted in Figure 7. It can be seen that the cell volume is reduced by no more than 1.6% relative to pristine $LiFeBO_3$, and that the majority of the change occurs for the b-axis. Although the changes in the β

dx.doi.org/10.1021/ic500169g | Inorg. Chem. 2014, 53, 6585−6595

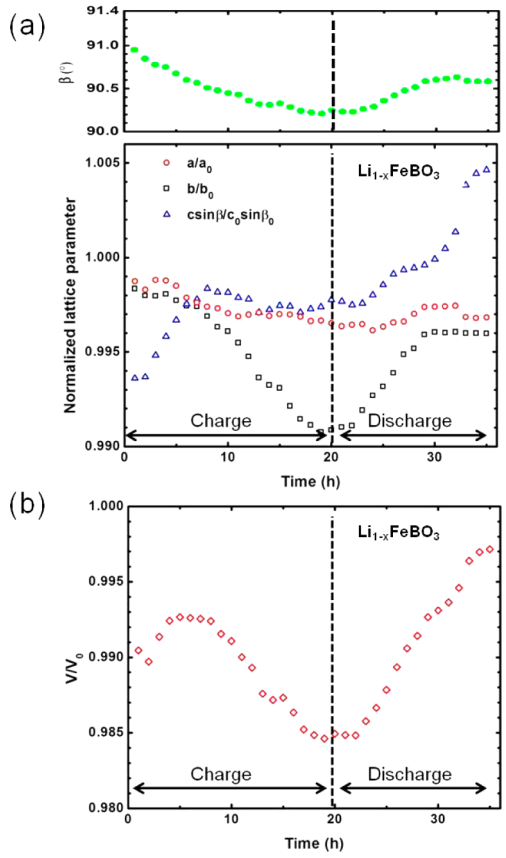

Figure 7. (a) Normalized lattice parameters of $Li_{1-x}FeBO_3$ during cycling. The distance c sin β is plotted instead of c because this product is the interlayer spacing. The top panel displays the progression of the β angle during cycling. The normalized volume is shown in (b). The normalization is against lattice parameters of $LiFeBO_3$ (a_0 = 5.1627 Å, b_0 = 8.9217 Å, c_0 = 10.1746 Å, β_0 = 91.381°, and V_0 = 468.50 Å^3).

angle are small, they represent a substantial movement toward the ideal value of 90°. These results are consistent with both theory and prior experimental measurements,[1,9] and again demonstrate that there are minimal changes in the $LiFeBO_3$ lattice during cycling.

The structural changes that occur during cycling in the low voltage process are not amenable to refinement due to the small volume fraction of the degraded phase (further discussed in the next section) and strong peak overlap with the major phase. The overall changes in peak position and intensity are quite small. However, it appears that discharge below 2 V causes a small increase in the c-lattice parameter of the electrochemically active phase during the lithiation process. This is evidenced by the reversible shift of the 004 peak (in the $C2/c$ subcell setting) in the XRD scans covering the low voltage redox process (scans 40−50, highlighted in red in Figure 8).

Electrochemical Activity of Degraded $LiFeBO_3$. Evidence for the electrochemical activity of the degraded phase, D-Li_dFeBO_3, is provided by the ^{7}Li NMR, in situ XRD, and electrochemical cycling experiments discussed above. This redox process occurs at low voltages (<2 V), and the D-Li_dFeBO_3−D-$Li_{d+y}FeBO_3$ redox couple is therefore expected to be the source of the 1.8 V plateau in the GITT data reported previously.[7] To better understand this electrochemical process, experiments focused on this low voltage region have been carried out to investigate the reversibility of this process, to probe the structural and compositional changes that this

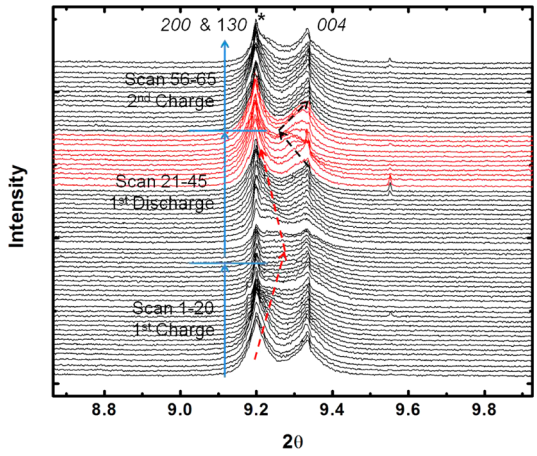

Figure 8. In situ XRD patterns of $LiFeBO_3$ during electrochemical cycling (65 scans in total), with a wavelength of ∼0.41 Å. The black curves represent the electrochemical processes occurring in $Li_{1-x}FeBO_3$, which primarily involve shifts of the 130 peak (obscured by the Fe_3BO_5 peak indicated by the "*" at 9.2°, details in Supporting Information Figure S5). This shift (indicated by red dotted line) is primarily induced by a change in the b-axis length for a monoclinic cell with a β angle close to 90°. The red curves (scans 40−50) highlight electrochemical processes occurring in D-Li_dFeBO_3, which involve 004 peak shifts. This shift (indicated by black dashed line) is driven by changes in the c-axis length.

process induces, and to explore the structural transformation pathways between the degraded and pristine phases. Accordingly, experiments have been carried out both on electrodes prepared from pristine $LiFeBO_3$ and on highly degraded samples prepared by heating $LiFeBO_3$ in air at 100 °C (for over a week) until the characteristic X-ray diffraction peaks of the pristine phase were suppressed.

The electrochemical performance of electrodes prepared from highly degraded samples (Figure 9) shares some common features with those prepared from pristine $LiFeBO_3$, even though there are substantial differences in the observed response. The degraded sample exhibits a net capacity of 140 mAh/g, which is divided between high voltage (∼2.8 V) and low voltage processes (∼1.8 V) in a manner similar to pristine

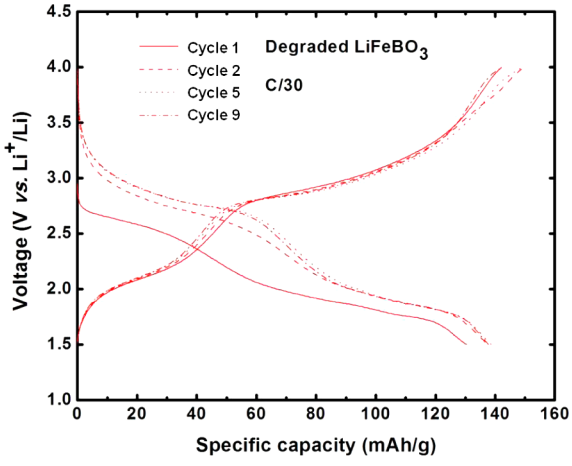

Figure 9. Electrochemical performance of highly degraded $LiFeBO_3$. Starting with discharge, the cell was cycled between 1.5 and 4 V at a rate of $C/30$ calculated on the basis of an assumed capacity of 220 mAh/g (i.e., full capacity of $LiFeBO_3$).

dx.doi.org/10.1021/ic500169g | Inorg. Chem. 2014, 53, 6585−6595

samples, but with a substantially larger fraction of the total capacity occurring at low voltage. The charge curves during the first nine cycles are closely superimposed, indicating good reversibility. In contrast, the initial discharge curves deliver a significantly reduced voltage relative to later cycles, indicating that the battery performance substantially improves upon cycling. These changes are much more pronounced in the high voltage regime (~2.8 V) associated with the pristine phase than in the low voltage regime (~1.8 V) associated with the degraded phase.

The differences between pristine and degraded $LiFeBO_3$ can be highlighted in dQ/dV plots (Figure 10). For the pristine

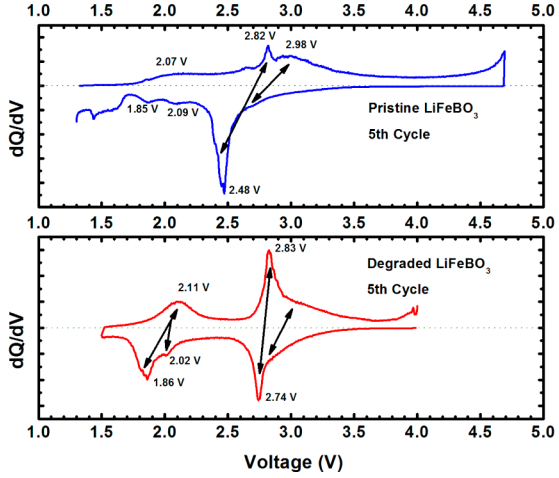

Figure 10. Comparison of fifth cycle dQ/dV data for electrodes prepared from pristine $LiFeBO_3$ (blue) and highly degraded $LiFeBO_3$ (red) showing that common high voltage (~2.8 V) and low voltage (~1.8 V) processes occur in both. Arrows indicate related charge and discharge events. First cycle data are shown in Figure S6 (Supporting Information).

sample, the primary ~2.8 V electrochemical features show up on charging at 2.82 V (sharp peak, likely associated with a two-phase reaction between $LiFeBO_3$ and $Li_{0.5}FeBO_3$) and at 2.98 V (broad peak, likely associated with $Li_{0.5}FeBO_3$–$Li_{0.5-x}FeBO_3$ solid solution), but these features shift substantially lower to 2.48 V on discharge and are found further from the thermodynamic plateau of ~2.8 V observed in GITT measurements. The degraded sample also shows electrochemical features in this potential range, which are attributed to the presence of a substantial quantity of $LiFeBO_3$ that has been oxidized (delithiated) but not degraded. Interestingly, the sharp features associated with the pristine $LiFeBO_3$ redox process (~2.8 V) on charge (2.83 V) and discharge (2.74 V) are separated less in the degraded sample than in the pristine sample, suggesting that a barrier to Li insertion has been removed. This is caused either by the use of lower cutoff voltage for charging, or likely by the further reduction of particle size of the pristine $LiFeBO_3$ phase via the degradation process.

The low voltage (~1.8 V) processes ascribed to the degraded phase are present in electrodes prepared from both pristine and degraded $LiFeBO_3$, although they are more clearly resolved in the degraded phase dQ/dV data, presumably due to the larger volume fraction of this low-voltage process. These features suggest that the degraded phase is present even in electrodes carefully prepared from the pristine phase, in agreement with the NMR results. Furthermore, the low voltage processes are very closely aligned for the two different samples and do not exhibit the large shift seen for the ~2.8 V process. The low operating voltage of the degraded $LiFeBO_3$ phase limits its potential use as a cathode candidate, although the substitution of Fe by other ions (Mn or Co) that have redox processes at higher voltages might result in electrochemistry suitable for battery applications. Additional solid-state NMR experiments focusing on the +218 ppm resonance of the degraded phase find the reversible low voltage electrochemistry results in this resonance decreasing in intensity with discharge below 2 V, and regaining intensity when charged to higher voltages (Figure S7 of the Supporting Information). The reversible ~1.8 V process must therefore be associated with the reversible removal and formation of the D-Li_dFeBO_3 degraded phase.

Structure of Degraded $LiFeBO_3$. The product of $LiFeBO_3$ degradation appears to be a phase that is structurally very similar to pristine $LiFeBO_3$, yet there is no evidence that pristine $LiFeBO_3$ can be regenerated from degraded $LiFeBO_3$ via electrochemical Li insertion at room temperature (see detailed discussion in the Supporting Information). The similarity of these phases can be inferred from both present and prior X-ray diffraction measurements that find only minor peak shifts and intensity changes when pristine $LiFeBO_3$ is subjected to degradation-inducing conditions. In the case of nanoparticles, this could be just prolonged air exposure, although for larger particles (>1 μm), heat treatment (100–200 °C) is generally required to eliminate the presence of X-ray diffraction peaks characteristic of pristine $LiFeBO_3$. The very different kinetics for different particle sizes suggests that the degradation process involves Li diffusion and Li loss through oxidation. We also find that the degradation process requires exposure to O_2, but not to H_2O, and therefore is unlikely to involve the formation of hydroxides or other hydrogen-containing species (Supporting Information Figure S10). This is further supported by neutron diffraction data collected on the degraded phase, which show no evidence of incoherent scattering from hydrogen in the background.

The structural similarity of pristine and degraded $LiFeBO_3$ on the local scale is apparent in neutron pair distribution function (PDF) studies, which were carried out on isotopic $^7LiFe^{11}BO_3$ samples to avoid problems with absorption. In contrast to X-ray scattering experiments, which are far more sensitive to Fe than the other elements in $LiFeBO_3$, neutron scattering techniques provide good sensitivity to Fe, B, and O but not Li (coherent scattering lengths in fm are ^{7}Li, −2.22; Fe, 9.45; ^{11}B, 6.65; O, 5.80). A comparison of the pair distribution function, $G(r)$, generated from the total scattering analysis of neutron diffraction data from both pristine and degraded $LiFeBO_3$ is given in Figure 11. The pairwise atomic correlations (i.e., peak positions) of these two samples in the real space $G(r)$ data are similar at all length scales. While peak intensities remain quite similar at distances corresponding to the local nearest neighbor coordination shells (1.3 Å for B–O bonds, 2.0–2.2 Å for Fe–O bonds, 2.4 Å for O–O pairs, and 3.1 Å for Fe–B neighbors in the cation planes), there are more noticeable differences in peak intensity at distances beyond 5 Å. The Fe–O bond lengths appear to be reduced after degradation, as expected for an oxidative process, which will result in higher valence iron with a smaller ionic radius. There is no evidence of peak shifts that would indicate a large change in the coordination environment of Fe, B, or O. The change in $G(r)$ peak intensities can therefore be attributed to small shifts

dx.doi.org/10.1021/ic500169g | Inorg. Chem. 2014, 53, 6585–6595

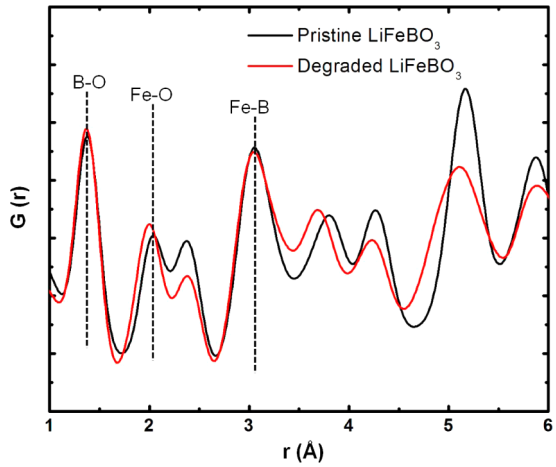

Figure 11. Neutron PDF data from pristine (black) and degraded (red) $LiFeBO_3$ powders, which were degraded by heating at 100 °C for 4 days until diffraction peaks from the pristine phase disappeared. A plot up to 50 Å can be found in Figure S11 of the Supporting Information.

in position or changes in occupancy of the original atomic sites in pristine $LiFeBO_3$.

Because both the Fe local environment and the overall nature of the borate framework appear to be essentially unchanged by the degradation process, the dramatically lower redox potential of the degraded phase (~1.8 vs ~2.8 V in the pristine $LiFeBO_3$) cannot be simply explained. The radical change in electrochemical properties is almost certainly related to structural changes that occur during the degradation process. Neutron diffraction experiments were therefore undertaken with the goal of determining the structure of the degraded phase. These refinements were made challenging by the relatively broad peaks and relatively weak diffraction peaks of the degraded phase, as well as the unavoidable coexistence of a delithiated phase whose diffraction peaks strongly overlap with those of the degraded phase. The inhomogeneity (i.e., the multiphase nature) of the degradation process can be clearly seen when $LiFeBO_3$ is heated isothermally at 200 and 240 °C under dry flowing O_2 (Figure 12). It can be seen in both cases that the

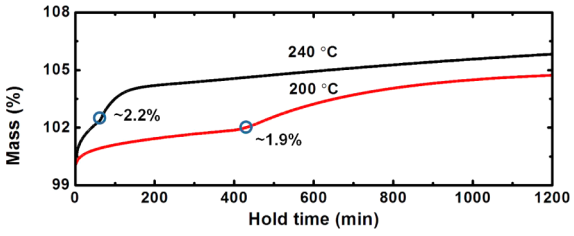

Figure 12. Thermogravimetric data of pristine $LiFeBO_3$ (micrometer-sized) collected isothermally under dry O_2 (25 mL/min) at 200 °C (red curve) or 240 °C (black curve). The rate of mass gain increases at ~2.0% mass gain during these two isothermal holds suggest a common structural transition associated with either delithiation or degradation.

reaction rate unexpectedly accelerates in the midst of the isothermal hold, suggesting that the initial partial oxidation of $LiFeBO_3$ (mass gain ~2.0%, which is substantially less than the expected gain of 6.6% for full oxidation) unlocks a distinct second oxidative process that can occur more rapidly despite the constant sample temperature. The conclusion that both degraded and delithiated $LiFeBO_3$ form during the degradation process is also supported by $^7Li/^{11}B$ NMR measurements, which are discussed in the Supporting Information.

The neutron diffraction data (Figure 13) from a degraded sample (200 °C, 5-day treatment) could not be appropriately fit

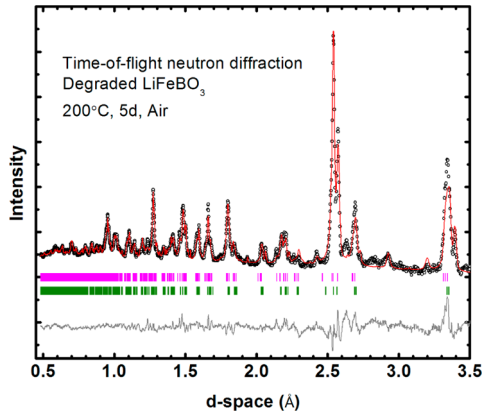

Figure 13. Rietveld refinements of degraded $LiFeBO_3$ by time-of-flight neutron diffraction (POWGEN). For clarity, only tick marks from the two main phases, degraded and delithiated $LiFeBO_3$, are shown in magenta and olive, respectively.

to a single monoclinic phase in Le Bail refinements, indicating the presence of an additional phase. Two-phase Le Bail refinements assuming the presence of both degraded (D-Li_dFeBO_3) and delithiated ($Li_{t-x}FeBO_3$) phases were successful in modeling the observed diffraction pattern with two separate lattices whose dimensions were both close to that of the pristine $LiFeBO_3$ monoclinic $C2/c$ subcell. One phase (a = 5.1393(15) Å, b = 8.7654(22) Å, c = 10.1254(23) Å; β = 90.332(26)°, V = 456.12(20) Å^3), later identified in Rietveld refinements as the degraded phase, had a refined crystallite size, which was 2 times larger than the other delithiated phase (a = 5.1333(18) Å, b = 8.8891(30) Å, c = 10.1633(21) Å; β = 90.351(19)°, V = 463.75(24) Å^3).

After identifying these two distinct phases, efforts were then made to explicitly model their diffraction peak intensities through Rietveld refinement. While the delithiated phase could be satisfactorily modeled by refining only the atomic positions of the non-Li atoms and the (reduced) site occupancies of the split Li sites, this was not the case for the degraded phase. The degraded phase modeled intensities only agreed with the experimental diffraction data when the occupancy of the Fe site was allowed reduced substantially below one, with a final refined site occupancy of 0.76(2). This indicates that the degradation process involves the displacement of Fe ions. This is fully consistent with the nature of the conditions that promote degradation (heating, oxidation in air). The smaller ionic radius and different coordination preferences of Fe^{3+} relative to the Fe^{2+} in pristine $LiFeBO_3$ are expected to provide a thermodynamic driving force, while mild heating provides extra activation energy for iron ions to escape their potential wells. This degradation pathway may also likely to be accessible for other transition metal borates, which are isostructural to $LiFeBO_3$, and perhaps may contribute to the source of the very poor electrochemical performance for both $LiMnBO_3$ and $LiCoBO_3$, although other factors such as poor electronic conductivity and/or the presence of the Jahn−Teller ion Mn^{3+} on charging $LiMnBO_3$ may also play a role.

dx.doi.org/10.1021/ic500169g | Inorg. Chem. 2014, 53, 6585−6595

There are two possible final resting places for the Fe ions that are lost from the Fe site of $LiFeBO_3$ during the degradation process. One likely position is at vacant Li sites, while the other possibility is the loss of Fe from the $LiFeBO_3$ framework. The original Li site becomes accessible primarily due to Li loss during the degradation process forming diamagnetic species surrounding the parent $LiFeBO_3$ particles, although a small amount of Li/Fe antisite disorder may also occur. When Fe was placed on the Li site in Rietveld refinements, the refined occupancy of this Fe site was 0.11(2), corresponding to only one-half of the ions lost from the majority site. Minimal differences in the quality of the refinement were found when this site was alternately tested to be fully vacant or to contain all of the Fe lost from the majority site. It is therefore not possible to discriminate between these two structural models (i.e., disordering of Fe onto the Li site and Fe loss) from the present neutron diffraction data. The same model for Fe occupying the Li site was also tested against the neutron PDF data (Supporting Information Figure S13); the refined distribution (0.56 Fe on the original Fe site and 0.11 Fe on the original Li site) was very similar to that obtained from Rietveld refinement of X-ray and neutron diffraction data. The Rietveld refinement results for degraded $LiFeBO_3$ are given in the Supporting Information (Tables S2–S4). Structural information is also provided for the delithiated phase that was included in the refinement, although small fraction of this phase (13 wt %) severely limits the accuracy of this refinement. Intriguingly, it was found that one of two split Li sites was fully occupied while the other was fully depopulated, providing both a putative stoichiometry ($Li_{0.5}FeBO_3$) and a rationale for the two-phase end member of the delithiation of $LiFeBO_3$. Although this result must be considered tentative given the limitations of the diffraction data, it does provide a trial structure whose importance to the delithiation process can be tested by density functional theory calculations.

Complementary information into the degradation process was obtained through high-resolution transmission electron microscopy (HRTEM) imaging of a single particle of the degraded phase (Figure 14). The interior of a degraded $LiFeBO_3$ particle can be very effectively modeled (box I) using the pristine $LiFeBO_3$ subcell in either a fully lithiated or a partially delithiated state (the image contrast is weakly sensitive to the Li content). This is consistent with prior EELS studies, which find divalent iron at the center of particles but more highly oxidized iron at the particle exterior.[7] Even accounting for changes in sample thickness, the next shell out from the particle center (box II) cannot be modeled with the same pristine structural model. However, this area can be very effectively modeled by a degraded structure in which iron is fully disordered (50/50) over the Fe and Li sites. The smaller degree of disorder suggested by Rietveld refinement (76/24) is also ineffective in modeling this region, suggesting that when there is a sufficient driving force to push Fe onto a Li site, there will be full randomization locally. Finally, the thin (~2 nm) outermost shell of the particle has less bright/dark contrast than the region assigned to the degraded phase. The very symmetrical HRTEM pattern here can perhaps be better simulated using a mixture of the hexagonal lattice of α-Fe_2O_3 (hematite) and the degraded $LiFeBO_3$ structure, as shown in the Supporting Information. The hexagonal structure of α-Fe_2O_3 has an in-plane lattice parameter of 5.04 Å, which is only 2% smaller than the pseudohexagonal lattice of pristine $LiFeBO_3$, and which almost perfectly matches the D-Li_dFeBO_3 lattice (5.07 Å in-plane for pseudohexagonal setting). It is possible that this outer layer contains Li, which has some solubility in α-Fe_2O_3,[18,19] although it is highly unlikely that borate groups are compatible with the close-packed oxygen framework of α-Fe_2O_3. The electrochemical behavior previously reported for α-Fe_2O_3 is not consistent with the voltage and capacities observed for $LiFeBO_3$ after degradation, further supporting the assignment of the 1.8 V electrochemical feature to the degraded $LiFeBO_3$ framework rather than a secondary phase of hematite.

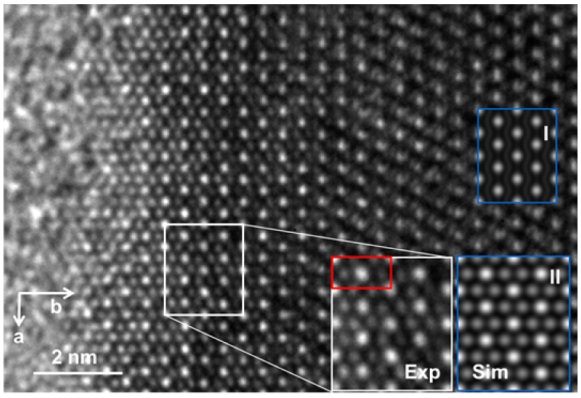

Figure 14. HRTEM image of a degraded $LiFeBO_3$ particle viewed in the [001] zone axis. Simulations are shown for pristine (I) and degraded (II) $LiFeBO_3$, with a zoom of the image shown next to the latter including a red box marking the relationship of the $LiFeBO_3$ unit cell to the image.

CONCLUSIONS

As summarized in Figure 15, it is found that the delithiation of $LiFeBO_3$ proceeds reversibly through first a two-phase reaction between $LiFeBO_3$ and Li_tFeBO_3 ($t \approx 0.5$) at ~2.8 V vs Li^+/Li and then through a solid solution between Li_tFeBO_3 and $Li_{t-x}FeBO_3$ ($0 < x < t$) at slightly higher potentials (2.8–3.2 V), although the full delithiation of $LiFeBO_3$ to form "$FeBO_3$" has not yet been experimentally demonstrated. For typical battery cells and normal cycling conditions, the solid-solution reaction begins well before the two-phase reaction is complete as a result of the large overpotentials commonly experienced. The degradation of $LiFeBO_3$ involves at least two separate processes that produce distinct degraded and delithiated phases, both of which share the same monoclinic framework as pristine $LiFeBO_3$. A key structural aspect of the degraded phase is the loss of iron from its original trigonal bipyramidal crystallographic site. TEM studies support the conclusion that the missing iron has moved onto what was formerly a Li site, although the complete loss of iron from the degraded phase (in the form of α-Fe_2O_3) cannot be definitively excluded. The degraded phase is oxidized relative to the pristine phase but still contains Li and can be reduced to contain only divalent iron when Li is intercalated at low voltages (<1.8 V). This degradation pathway is also expected to be accessible for other transition metal borates such as $LiMnBO_3$ and $LiCoBO_3$, and could be responsible for the poor electrochemical performance of these phases if the degradation pathway of losing transition metal from the bipyramidal site can occur at room temperature.

dx.doi.org/10.1021/ic500169g | Inorg. Chem. 2014, 53, 6585–6595

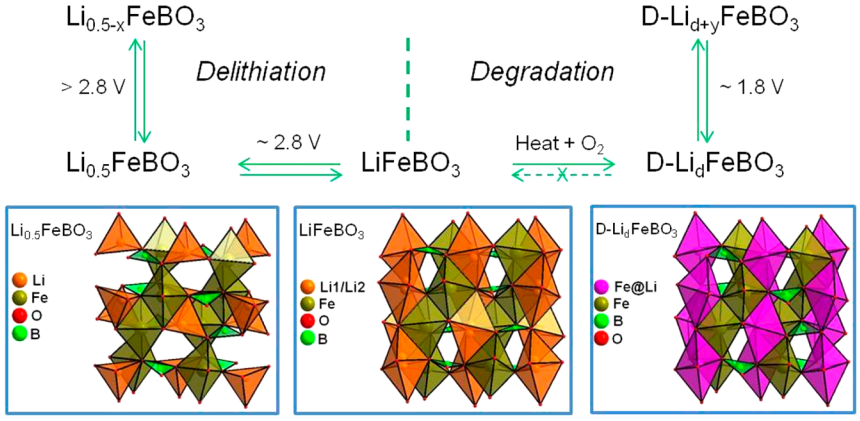

Figure 15. Summary of the structural transformation pathways of $LiFeBO_3$ during delithiation and degradation.

■ ASSOCIATED CONTENT

Supporting Information

In situ XAS/XRD, ex situ NMR, the electrochemical performance comparison of $LiFeBO_3$ and D-Li_dFeBO_3, and the structural information about the degraded $LiFeBO_3$ (including the cif file and inp file for Rietveld refinement in TOPAS). This material is available free of charge via the Internet at http://pubs.acs.org.

■ AUTHOR INFORMATION

Corresponding Authors

*E-mail: cpg27@cam.ac.uk.
*E-mail: kpete@bnl.gov.

Present Address

⊥Department of Energy and Materials Engineering, Dongguk University-Seoul, Seoul, 100-715, Republic of Korea.

Notes

The authors declare no competing financial interest.

■ ACKNOWLEDGMENTS

This work was supported by the Northeastern Center for Chemical Energy Storage, an Energy Frontier Research Center funded by the U.S. DOE, BES under award no. DE-SC0001294, including matching support from NYSTAR-NYSDED. The Neutron Bragg diffraction and NPDF studies were supported by the Office of Basic Energy Sciences, U.S. Department of Energy, at the Spallation Neutron Source, Oak Ridge National Laboratory under contract DE-AC05-00OR22725 with UT Battelle. Dr. Mikhail Feygenson (NOMAD) and Dr. Ashfia Huq (POWGEN) are acknowledged for their help in the NPDF and neutron powder diffraction data collection. The in situ XAS study was carried out at National Synchrotron Light Source (NSLS), and the use of the NSLS, Brookhaven National Laboratory, was supported by the U.S. Department of Energy, Office of Science, Office of Basic Energy Sciences, under contract no. DE-AC02-98CH10886. TEM studies were carried out at the Center for Functional Nanomaterials, Brookhaven National Laboratory, which is supported by the U.S. Department of Energy, Office of Basic Energy Sciences, under contract no. DE- AC02-98CH10886. The in situ XRD study done at Argonne and use of the Advanced Photon Source (APS), an Office of Science User Facility operated for the U.S. Department of Energy, Office of Science, by Argonne National Laboratory, were supported by the U.S. Department of Energy under contract no. DE-AC02-06CH11357. Kamila M. Wiaderek is acknowledged for her help with the experimental setup during measurements at 11-BM. We thank Dr. Zhehong Gan for useful discussion on the implementation of the pj-MATPASS NMR pulse sequence.

■ REFERENCES

(1) Yamada, A.; Iwane, N.; Harada, Y.; Nishimura, S.; Koyama, Y.; Tanaka, I. *Adv. Mater.* **2010**, *22*, 3583−3587.
(2) Tao, L.; Rousse, G.; Chotard, J. N.; Dupont, L.; Bruyere, S.; Hanzel, D.; Mali, G.; Dominko, R.; Levasseur, S.; Masquelier, C. *J. Mater. Chem. A* **2014**, *2*, 2060−2070.
(3) Barpanda, P.; Yamashita, Y.; Yamada, Y.; Yamada, A. *J. Electrochem. Soc.* **2013**, *160*, A3095−A3099.
(4) Kim, J. C.; Moore, C. J.; Kang, B.; Hautier, G.; Jain, A.; Ceder, G. *J. Electrochem. Soc.* **2011**, *158*, A309−A315.
(5) Yamada, A.; Iwane, N.; Nishimura, S.; Koyama, Y.; Tanaka, I. *J. Mater. Chem.* **2011**, *21*, 10690−10696.
(6) (a) Legagneur, V.; An, Y.; Mosbah, A.; Portal, R.; La Salle, A. L.; Verbaere, A.; Guyomard, D.; Piffard, Y. *Solid State Ionics* **2001**, *139*, 37−46. (b) Dong, Y. Z.; Zhao, Y. M.; Shi, Z. D.; An, X. N.; Fu, P.; Chen, L. *Electrochim. Acta* **2008**, *53*, 2339−2345.
(7) Bo, S. H.; Wang, F.; Janssen, Y.; Zeng, D. L.; Nam, K. W.; Xu, W. Q.; Du, L. S.; Graetz, J.; Yang, X. Q.; Zhu, Y. M.; Parise, J. B.; Grey, C. P.; Khalifah, P. G. *J. Mater. Chem.* **2012**, *22*, 8799−8809.
(8) Janssen, Y.; Middlemiss, D. S.; Bo, S. H.; Grey, C. P.; Khalifah, P. G. *J. Am. Chem. Soc.* **2012**, *134*, 12516−12527.
(9) Seo, D. H.; Park, Y. U.; Kim, S. W.; Park, I.; Shakoor, R. A.; Kang, K. *Phys. Rev. B* **2011**, *83*, 205127.
(10) Grey, C. P.; Dupre, N. *Chem. Rev.* **2004**, *104*, 4493−4512.
(11) Ravel, B.; Newville, M. *J. Synchrotron Radiat.* **2005**, *12*, 537−541.
(12) Borkiewicz, O. J.; Shyam, B.; Wiaderek, K. M.; Kurtz, C.; Chupas, P. J.; Chapman, K. W. *J. Appl. Crystallogr.* **2012**, *45*, 1261−1269.
(13) Neuefeind, J.; Feygenson, M.; Carruth, J.; Hoffmann, R.; Chipley, K. K. *Nucl. Instrum. Methods Phys. Res., Sect. B* **2012**, *287*, 68−75.
(14) Hung, I.; Zhou, L. N.; Pourpoint, F.; Grey, C. P.; Gan, Z. H. *J. Am. Chem. Soc.* **2012**, *134*, 1898−1901.
(15) Le Toquin, R.; Paulus, W.; Cousson, A.; Prestipino, C.; Lamberti, C. *J. Am. Chem. Soc.* **2006**, *128*, 13161−13174.
(16) David, W. I. F. *J. Appl. Crystallogr.* **2001**, *34*, 691−698.
(17) Stone, K. H.; Lapidus, S. H.; Stephens, P. W. *J. Appl. Crystallogr.* **2009**, *42*, 385−391.
(18) Larcher, D.; Bonnin, D.; Cortes, R.; Rivals, I.; Personnaz, L.; Tarascon, J. M. *J. Electrochem. Soc.* **2003**, *150*, A1643−A1650.
(19) Larcher, D.; Masquelier, C.; Bonnin, D.; Chabre, Y.; Masson, V.; Leriche, J. B.; Tarascon, J. M. *J. Electrochem. Soc.* **2003**, *150*, A133−A139.

dx.doi.org/10.1021/ic500169g | *Inorg. Chem.* 2014, 53, 6585−6595